



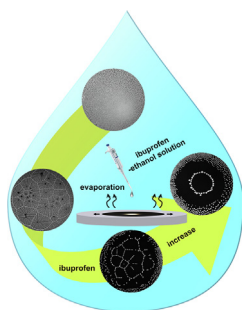
Evaporation-induced fractal patterns: A bridge between uniform pattern and coffee ring

Fushuai Wang, Quanzi Yuan*

State Key Laboratory of Nonlinear Mechanics, Institute of Mechanics, Chinese Academy of Sciences, Beijing 100190, People's Republic of China
School of Engineering Science, University of Chinese Academy of Sciences, Beijing 100049, People's Republic of China



GRAPHICAL ABSTRACT



ARTICLE INFO

Article history:

Received 20 October 2022
Revised 17 January 2023
Accepted 20 January 2023
Available online 24 January 2023

Keywords:

Evaporation
Drop
Self-assembled pattern
Contact line
Film stability

ABSTRACT

Hypothesis: The rich variety of patterns induced by evaporating drops containing particles has significant guidance for coating processes, inkjet printing, and nanosemiconductors. However, most existing works construct a uniform pattern by suppressing the coffee ring effect, and establishing the connection between them is still an academic challenge.

Experiments: We report uniform, polygonal, and coffee ring patterns obtained by adjusting the solute concentration that sets in when an ethanol drop with dissolved ibuprofen is deposited on a silicon wafer. **Findings:** Pattern formation involves rich hydrodynamic events: spreading, evaporative instability, dewetting, film formation, and particle deposition. Based on the distinct multiscale properties, this series of patterns is directly connected from the perspective of fractal geometry, which allows us to name them “fractal deposition patterns”. A theoretical model considering film stability is established to explain the mechanism behind pattern formation, which is well verified by experiments. This work has presented a unique strategy that can directly connect uniform, polygonal, and coffee ring patterns under the same physics, hoping to provide instructive guidance for practical applications.

© 2023 Elsevier Inc. All rights reserved.

* Corresponding author at: State Key Laboratory of Nonlinear Mechanics, Institute of Mechanics, Chinese Academy of Sciences, Beijing 100190, People's Republic of China.

E-mail address: yuanquanzi@lnm.imech.ac.cn (Q. Yuan).

1. Introduction

The evaporation of a drop is a simple everyday observation. However, it has promoted the development of many fascinating research topics, such as contact line dynamics [1], evaporation-induced phase transition [2], and particle deposition [3,4]. For example, when we exercise vigorously on a very hot summer day, much perspiration will occur on the skin's surface. If we

observed carefully, dissolved residues will be left around the edge to form a ring-like pattern after the small perspiration drop adhered to the skin evaporates. This has come to be known as the coffee ring phenomenon, which is interpreted as the capillary flow caused by strong evaporation of the three-phase contact line (TPCL) bringing residues to the edge [3,4]. In contrast, a large drop falls due to gravity, leaving a thin film that adheres to the skin. Under the external disturbance, the thin film ruptures, randomly forming many dry holes. Then, dry holes expand on the skin by forming ridges, and when they meet, several temporary polygonal patterns appear. The mechanism behind the rupture of the film corresponds to the amplification of capillary waves, i.e., the spinodal decomposition [5,6].

This rich phenomenon in life may enlighten us on the construction of surface patterns needed in nanosemiconductors [7], inkjet printing [8], coating processes [9], and other technical fields. In particular, it is necessary to construct a uniform pattern. However, the ubiquity of the coffee ring effect undoubtedly poses a significant challenge [10,11]. In general, the coffee ring phenomenon arises from the strong evaporative flux at the pinned TPCL and the weak Marangoni convection at the liquid–vapor interface [3,12,13]. The substrate wetting properties are modified by physical or chemical methods to control the motion of the TPCL [14,15]. In addition, researchers have changed the shape of particles to affect particle–particle interactions [10] or applied a voltage to generate a radially inward electroosmotic flow to weaken the radially outward capillary flow [16]. The capillary flow is greatly weakened or even eliminated by performing the particle deposition process on a prefabricated confined interface [17–19]. More ingeniously, by varying the substrate stiffness, i.e., without a direct compromise of the drop, the moving state of the contact line is adjusted to obtain a uniform pattern and even achieve the transition from a centralized multilayer pattern to a uniform monolayer pattern [20–22]. Marangoni convection, an interface flow phenomenon driven by the surface tension gradient, originates from uneven temperature or concentration distributions [23]. For drops with high volatility, the cooling effect of evaporation, which must be considered, results in an uneven temperature distribution [24,25]. However, the volatile drop actively wets the substrate, and this effect gradually becomes weak as the drop becomes thin. In addition, the fast evaporation at the TPCL leads to instability, such as wrinkling of the liquid–vapor interface [26,27]. For low volatility drop evaporation, the surface tension gradient caused by temperature is rare [12], which may be attributed to the rapid disappearance of the temperature difference due to the good heat conduction caused by the convection inside the drop. Therefore, uniform patterns are difficult to achieve in practice by adjusting the temperature distribution. It is relatively easy to achieve that by adjusting the composition to build the surface tension gradient, and the flow field inside the drop can be significantly changed, affecting the particle deposition process [28]. To the best of our knowledge, most current studies on modifying the coffee ring effect are based on the above two aspects. Various issues interact here, making the obtention of a uniform pattern more complicated. Hence, it is particularly important to seek other strategies to construct uniform patterns, and achieving various deposition patterns under the same physics, i.e., constructing and explaining arbitrary self-assembled patterns using limited experimental and theoretical models, remains a key challenge.

Here, we realized the construction and unification of uniform, polygonal, and coffee ring patterns under the same experimental model, considering a simple but ingenious system made of an ethanol drop with dissolved ibuprofen deposited on a smooth silicon wafer. Through the combination of a theoretical model and experimental methods, a series of rich hydrodynamic behaviors shown in the experiment is analyzed in detail, and the mechanism of

the formation of various patterns is revealed. The theoretical model agrees with the experimental results. In addition, this series of deposition patterns exhibits distinct multiscale properties in the geometry, prompting us to establish the bridge between uniform patterns and coffee rings through fractal dimensions, where polygonal patterns are the intermediate state. Therefore, we name the series of patterns “fractal deposition patterns”. To the best of our knowledge, this is the first report to unify the uniform pattern and coffee ring under the same physics, hoping to provide instructive guidance for practical applications.

2. Experimental section

2.1. Materials

The solution, whose concentration ranges from 0 to 0.5 g mL⁻¹, is prepared by dissolving ibuprofen (GC, ≥98 %, Shanghai Aladdin Biochemical Technology Co., Ltd.) in ethanol (AR, ≥99.7 %, Tianjin Dingshengxin Chemical Industry Co., Ltd). The substrate adopts a smooth and clean silicon wafer, with a root-mean-square roughness on the order of 10⁻¹ nm (Fig. S1). The volume of drops is 6.0 μl, deposited on the substrate by a pipette. Here, the drop volume does not significantly affect the main features of the final deposition pattern, and Fig. S2 shows an example of 0.04 g mL⁻¹, whose details will be discussed in Section 3. The experiments are carried out at room temperature $RT = 298 \pm 2$ K and relative humidity $RH = 17 \pm 2$ %. It is worth noting that low humidity can help to greatly reduce the oxidation of silicon wafers, thus avoiding chemical reactions with ibuprofen molecules with carboxyl groups [29]. The surface tension and the contact angle were tested by a contact angle measurement system (Kruss: DSA30s), and the viscosity of the mixed solution was tested by a viscometer (BROOKFIELD: DV-III Ultra). The whole processes are recorded by the microscopic imaging system (15 fps) from the top view, and the deposition patterns are photographed and stored by a single-lens reflex camera (Canon EOS 80D). All experiments are performed on a vibration isolator to minimize errors caused by the external environment.

2.2. Film thickness measurements

It can be seen from Fig. 2 that during film dewetting, i.e., after the film ruptures, ibuprofen is precipitated and collected at the ridge (the edge of the hole), and the interference color of the film remains unchanged. Light energy is proportional to the gray-scale value, which can reflect the change of film thickness [27,30]. The gray-scale value measurements show that it first decreases with time, and then tends to be flat after the film ruptures (Fig. S3). Once the film is formed, the rapid evaporation of ethanol results in the decrease of film thickness until the film is almost composed of ibuprofen, whose thickness fluctuates near an equilibrium value due to inertia. Therefore, the average thickness of the film e_0 could be measured by the spectroscopic ellipsometer (J.A. Woollam RC2 -D). The fitted relation between e_0 and c_0 (<0.1 g mL⁻¹) is given as $e_0 = 162.5 + 21 \times \ln c_0$ (Fig. S4). When $c_0 = 0.1$ g mL⁻¹, $e_0 = 128.69 \pm 0.229$ nm; and when $c_0 = 0.2$ g mL⁻¹, $e_0 = 1587.97 \pm 124.079$ nm.

2.3. Drop profile measurements

Spectral ellipsometry combined with red light interference experiments (Fig. 1a) are employed to determine the profile of the drop.

$$h(r, t) = e_0 + \frac{m\lambda_R}{2n}, \quad (1)$$

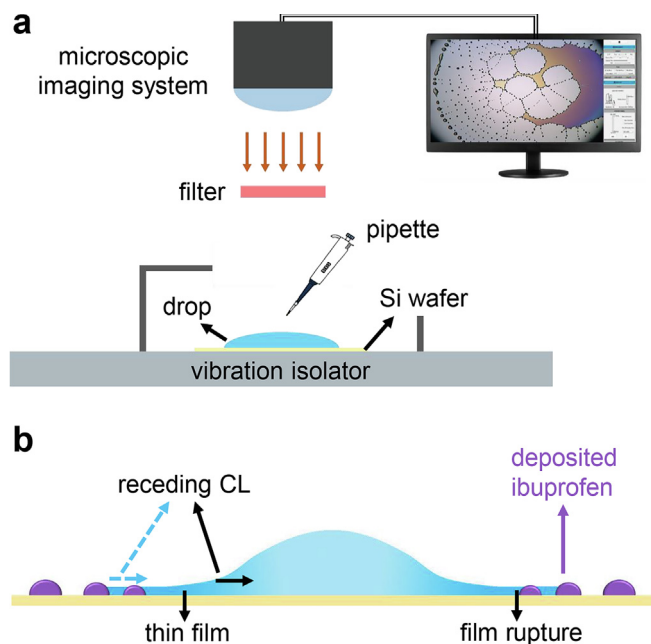


Fig. 1. Schematic illustration of the experimental setup and process. (a) A 6.0 μl ethanol drop containing ibuprofen is dropped on the silicon wafer, which is visualized and recorded by the microscopy system (details in the Experimental Section). Fig. 1b schematically depicts a series of rich hydrodynamic events experienced by the drop on the silicon wafer from a side view, such as spreading, evaporative instability, dewetting, film formation, and particle deposition. Note that the whole experimental setup is clear and easy to operate, but the complexity it exhibits arises from the physicochemical properties of the involved materials: ethanol is a fast-volatile organic solvent; ibuprofen is nonvolatile and dissolves well in ethanol, whose saturation concentration is approximately 0.1 g mL^{-1} at room temperature; the amount of ibuprofen can change the physicochemical properties of the mixed solution, such as the surface tension and the viscosity; and ibuprofen precipitated from ethanol tends to form spherical clusters, which are conducive to self-assembly into various patterns.

where $h(r, t)$ is the height of the drop, e_0 is the average thickness of the film measured by spectral ellipsometry, m is the number of interference fringes, $\lambda_R = 635 \text{ nm}$ is the wavelength of red light, and $n = 1.096$ is the refractive index of ethanol at 298 K.

3. Results and discussion

3.1. Pattern formation in the evaporating drop

A 6.0 μl ibuprofen-ethanol (nonvolatile solute-volatile solvent) drop is deposited onto a smooth, clean silicon wafer (Fig. 1a), which is visualized and recorded by the microscopy system (details in the Experimental Section). Fig. 1b schematically depicts a series of rich hydrodynamic events experienced by the drop on the silicon wafer from a side view, such as spreading, evaporative instability, dewetting, film formation, and particle deposition. Note that the whole experimental setup is clear and easy to operate, but the complexity it exhibits arises from the physicochemical properties of the involved materials: ethanol is a fast-volatile organic solvent; ibuprofen is nonvolatile and dissolves well in ethanol, whose saturation concentration is approximately 0.1 g mL^{-1} at room temperature; the amount of ibuprofen can change the physicochemical properties of the mixed solution, such as the surface tension and the viscosity; and ibuprofen precipitated from ethanol tends to form spherical clusters, which are conducive to self-assembly into various patterns.

3.1.1. Drop spreading

The dynamic process and the evolution law are clearly presented in Fig. 2. Fig. 2a–d shows the dynamic behaviors of several typical ethanol drops with different initial ibuprofen concentrations c_0 (g mL^{-1}) spanning four orders of magnitude on the silicon wafer, i.e., 0.0005 g mL^{-1} , 0.003 g mL^{-1} , 0.04 g mL^{-1} , and

0.3 g mL^{-1} (Movie S1–S4, respectively). Once the drop is released, it spreads on the substrate immediately (Fig. 2a1, b1, c1, and d1) until it reaches the maximum spreading radius (Fig. 2a3, b3, c3, and d3). The viscosity changes from 1.0 to 2.4 cp due to the addition of ibuprofen (Fig. S5). Based on the viscosity of liquid μ , the density of liquid ρ , the characteristic length L , the characteristic velocity U , the gravitational acceleration g , and the surface tension γ of liquid, the spreading speed reaches a maximum when t is at most 0.2 s. In this early stage, the gravitational effect should be considered because the Bond number $Bo = \rho g L^2 / \gamma \sim 10^{-1}$. The Ohnesorge number $Oh = \mu / (\rho L \gamma)^{1/2} \sim 10^{-3}$, is less than 1, and the Reynolds number $Re = \rho U L / \mu \sim 10^1$, is greater than 1. In addition, the viscous forces could be neglected compared with the inertia, which is consistent with the volatile low viscosity ethanol [31]. Therefore, the balance of the driving gravitational forces and the resisting inertial forces resulting in a large initial spreading speed.

In the later stage ($t > 0.2\text{s}$), the height of the center of the spreading drop h_0 becomes very small $h_0/R \sim 10^{-2}$. Here, the gravitational effect is negligible ($Bo \sim 10^{-2} \ll 1$). Fig. 3a summarizes the variation in the spreading radius R (mm) with time t ($\geq 0.2\text{s}$) at various c_0 . Judging from the convex shape on the curve, the spreading law of ibuprofen-ethanol drops is similar to the spreading of the pure ethanol drop (black line of Fig. 3a), which first spreads fast, then gradually slows, until it stops. However, the addition of ibuprofen appears to speed up spreading, which indicates that ibuprofen modifies the wetting properties of the mixed drop on the silicon wafer.

Explaining the spreading of the volatile drop is still a challenge because of the combined effects of evaporation, dynamic surface tension (influence of the initial contact angle on the unbalanced surface tension at the contact line), the Marangoni effect, inertial force ($Oh \cdot 10^{-3} \ll 1$), and particle deposition [32]. In this work, we take the spreading of a pure ethanol drop as the reference system to focus on the influence of the addition of ibuprofen. Scaling law analysis is used to describe the above phenomenon. By fitting the experimental data, it is found that the spreading radius R (mm) and time t (s) satisfy a scaling relation, $R \propto t^n$ ($n = 0.29 \sim 0.37$, Fig. 3b), where the scaling exponent n represents the spreading properties of the solid-liquid system. Fig. 3b shows that n changes nonlinearly with increasing c_0 , but n is larger than that of pure ethanol (black asterisk). When $c_0 < 0.008 \text{ g mL}^{-1}$, n is very sensitive to c_0 . It can be seen from Fig. 2a2–a3 and 2b2–b3 that the spreading front is surrounded by the precipitated ibuprofen particles, that is, the ibuprofen is in a supersaturated state at the drop edge. Surface tension measurements show that the increase is linear with the addition of ibuprofen when c_0 exceeds the saturation concentration $c_{\text{sat}} \sim 0.1 \text{ g mL}^{-1}$ (the red line of Fig. 3c); that is, a constant surface tension gradient is applied at the spreading front. In addition, the initial contact angle of the drop θ_0 increases with c_0 ($< 0.008 \text{ g mL}^{-1}$), indicating that the resistance of the dynamic surface tension effect is weakened. Therefore, the Marangoni effect and dynamic surface tension effect jointly accelerate spreading. When $0.008 < c_0 < 0.1 \text{ g mL}^{-1}$, according to the change in the surface tension (Fig. 3c) and the initial contact angle (Fig. 3d), the scaling exponent n should continue to increase with c_0 , but remain at 0.31. We suggest that the increased size of ibuprofen particles at the drop front (Fig. 2c2–c3) begins to hinder further spreading. Next, when $c_0 > 0.1 \text{ g mL}^{-1}$, the increase in θ_0 further weakens the resistance of the dynamic surface tension effect. In addition, the rapid evaporation of ethanol leads to a concentration gradient from the bulk to the edge of the drop. Thus, the action range of the Marangoni effect changes from the edge to the

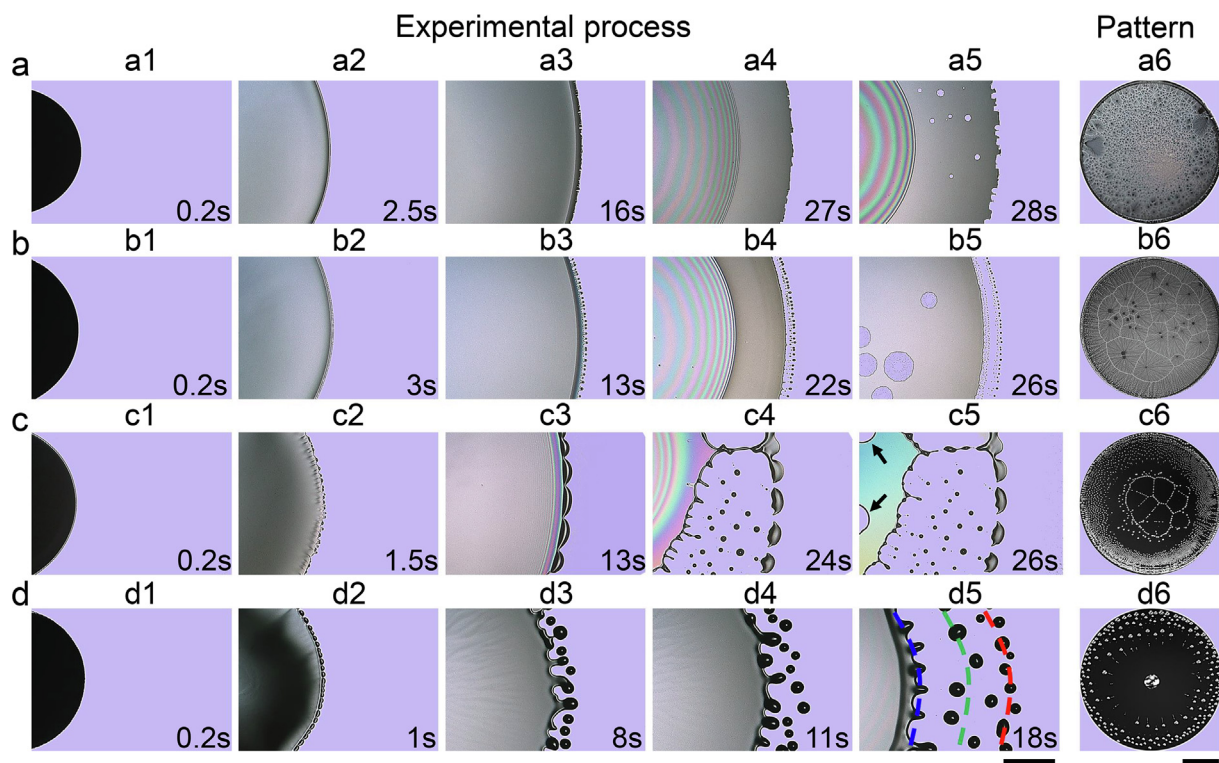


Fig. 2. Experimental process of the formation of deposition patterns. The evolution of ethanol drops with different initial ibuprofen concentrations on the silicon wafer, (a) 0.0005 g mL^{-1} , (b) 0.003 g mL^{-1} , (c) 0.04 g mL^{-1} , and (d) 0.3 g mL^{-1} . Snapshots (a1–a5, b1–b5, c1–c5, and d1–d5) capture all the hydrodynamic events: spreading, evaporative instability, dewetting, film formation, and particle deposition. The scale bars are 1 mm in the “experimental process” and 5 mm in the “pattern”.

whole bulk. As shown in Fig. 2d3–d4, radially outward folds at the liquid–vapor interface are observed, which are driven by the competition between the Marangoni stress and the restoring gravity effect [27,33].

In general, the change in the scaling exponent n is positively correlated with the maximum spreading radii [34,35]. However, this is not the case here, where the maximum spreading radii under the addition of ibuprofen are all between 9.2 mm and 10.3 mm (Fig. 3a and S6). The difference is negligible compared to the maximum spreading radii. We believe that this is determined by the inherent property of rapid ethanol evaporation.

3.1.2. Evaporative instability - fingering instability

At high c_0 , the spreading ends in a very short period, as shown by the magenta line of Fig. 3a (0.3 g mL^{-1}), where the total spreading time decreases by approximately 50 %, leading to most ethanol remaining in the bulk of the drop. Then, under the coupling between the rapid pinned TPCL and the strong Marangoni effect, the remaining ethanol-ibuprofen is released in the form of the ejection, where the drop bulk plays the role of a reservoir (Fig. 2d3). Once the TPCL is depinned and starts to recede, the ejection stops. In contrast, in the isopropyl alcohol–water (liquid–liquid) combination, when the drop has reached its maximal spreading radius, the TPCL is not pinned and starts to recede while continually ejecting drops [27]. Difficultly arises in the solid–liquid combination, as the precipitated particles will in turn affect the motion of the TPCL, thereby complicating matters [36].

In fact, the phenomenon of particle ejection is an accelerated fingering instability. For $c_0 \leq 0.2 \text{ g mL}^{-1}$, complete fingers are observed at the spreading front (Fig. 2a–c) [26,37,38]. For the spreading of pure ethanol on the silicon wafer, fingers also emerge at the spreading front, whose size is on the order of $10 \mu\text{m}$ (Fig. S7). This contrasts with the spreading of a pure isopropanol drop on the

same substrate, which is due to the faster volatility of ethanol [26,39]. The mechanism behind this phenomenon is already well understood, in which Rayleigh–Plateau instability leads to the breakup of a continuous rim into small drops [37,38], acting as progenitors to the emerging fingers. Fig. 3e depicts the finger size S (the length L and the wavelength W) changing with initial ibuprofen concentration c_0 at the same moment ($t = 9 \text{ s}$). The size of the fingers spans from 10^1 to $10^2 \mu\text{m}$. S increases with c_0 , satisfying the scaling $c_0^{1/3}$ (red solid line of Fig. 3e). The fingers are mainly composed of ibuprofen and are presented in a hemispherical shape (Fig. S8). The evaporation rate of ethanol is a constant at atmospheric pressure. The total mass of precipitated ibuprofen over the same period $V_e c_0 = N \rho V^*$, where V_e is the volume of evaporated ethanol, N is the number of fingers, ρ is the density of ibuprofen, and V^* is the volume of a finger. V^* is proportional to S^3 ; hence, the finger size will be $S \propto c_0^{1/3}$.

3.1.3. Drop dewetting

Combining red-light interference experiments and spectral ellipsometry, the profile during drop dewetting is explored (details in the Experimental Section). Fig. 4a and b depict the evolution of the drop profile at $c_0 = 0.001$ and 0.04 g mL^{-1} , respectively, showing that the shape of the drop transitions from the pancake to the spherical crown during dewetting. The pancake shape of the drop is apparent as c_0 increases (Fig. 4a, b, and S9). Fig. 4c shows that the evaporation mode has undergone a mixed mode where both the contact angle θ_d and contact radius R_d change. In the first 40 % of the total detwetting time, R_d is no sensitive with time and the corresponding θ_d decreases rapidly. When θ_d reaches approximately 0.05° , the drop begins dewetting. In the next 60 % of the total detwetting time, θ_d changes slowly and R_d decreases

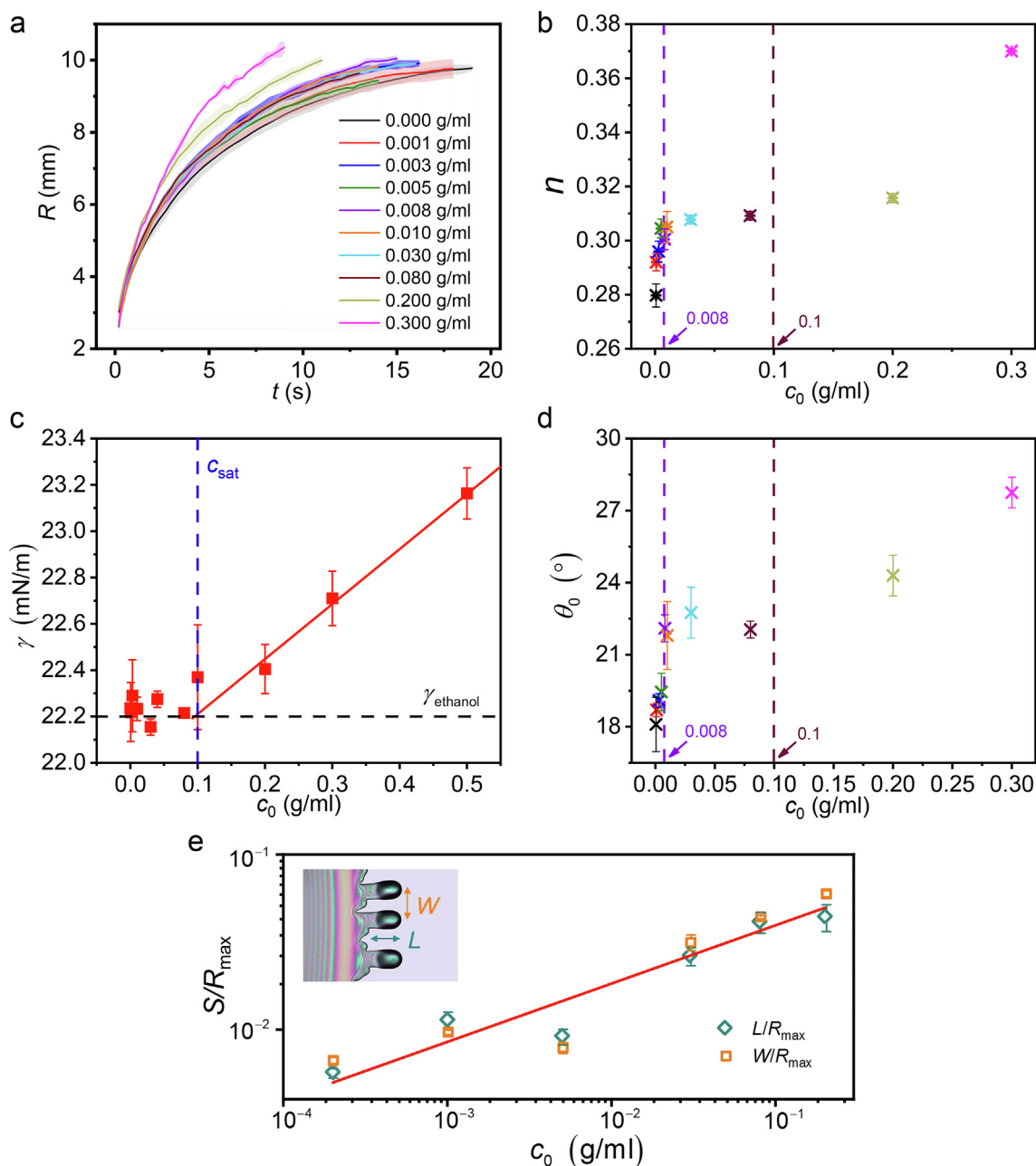


Fig. 3. Spreading law of ethanol drops with different initial ibuprofen concentrations c_0 on the silicon wafer. (a) Spreading radius R of drops as a function of time t , satisfying a scaling relation, $R \propto t^n$. (b) The scaling exponent n varies with c_0 . (c) The surface tension γ varies with c_0 , where c_{sat} represents the saturation concentration of ibuprofen. (d) The initial contact angle θ_0 varies with c_0 . (e) Finger size S (wavelength W and length L of the fingers) as a function of c_0 , plotted in double logarithmic coordinates. Discrete dots represent the experimental results, and the red solid line represents the theoretical prediction $S \propto c_0^{1/3}$. (For interpretation of the references to color in this figure legend, the reader is referred to the web version of this article.)

rapidly. This change of R_d and θ_d is caused by the fast evaporation of ethanol.

3.1.4. Film formation and dewetting

After drop dewetting, a film is left on the substrate. It is worth noting that the addition of ibuprofen accelerates the spreading ($c_0 < 0.1 \text{ g mL}^{-1}$), generating a narrow edge with visible width (0–0.36 mm) (Fig. 2a3, b3, and c3). Compared with the maximum spreading radius, the edge width is negligible. However, the narrow edge is a precursor of the subsequently formed film, whose two contact lines are located on the substrate and the edge. The contact line on the edge recedes rapidly, and the edge gradually

grows into a film left on the substrate (Fig. 2a4, b4, and c4). External disturbances affect the film stability, causing fluctuations on the film surface. When the thinnest regions of the film rupture, a dry hole will appear, expanding on the substrate by forming a ridge (indicated by the arrow in Fig. 2c5). Multiple ridges meet, and ibuprofen particles deposit, finally forming a uniform or polygonal pattern (Fig. 2a6, b6, and c6), which is determined by the scale of the distance between polygons (detailed in Section 3.2). The radius of holes R_{hole} varies linearly with time t captured from experiments, indicating that the film dewets the substrate at a constant velocity (Fig. 4d). When $c_0 > 0.1 \text{ g mL}^{-1}$, the narrow edge disappears, and the entire drop begins to dewet the substrate while the particle ejection stops. With the evaporation of ethanol, the shape of the

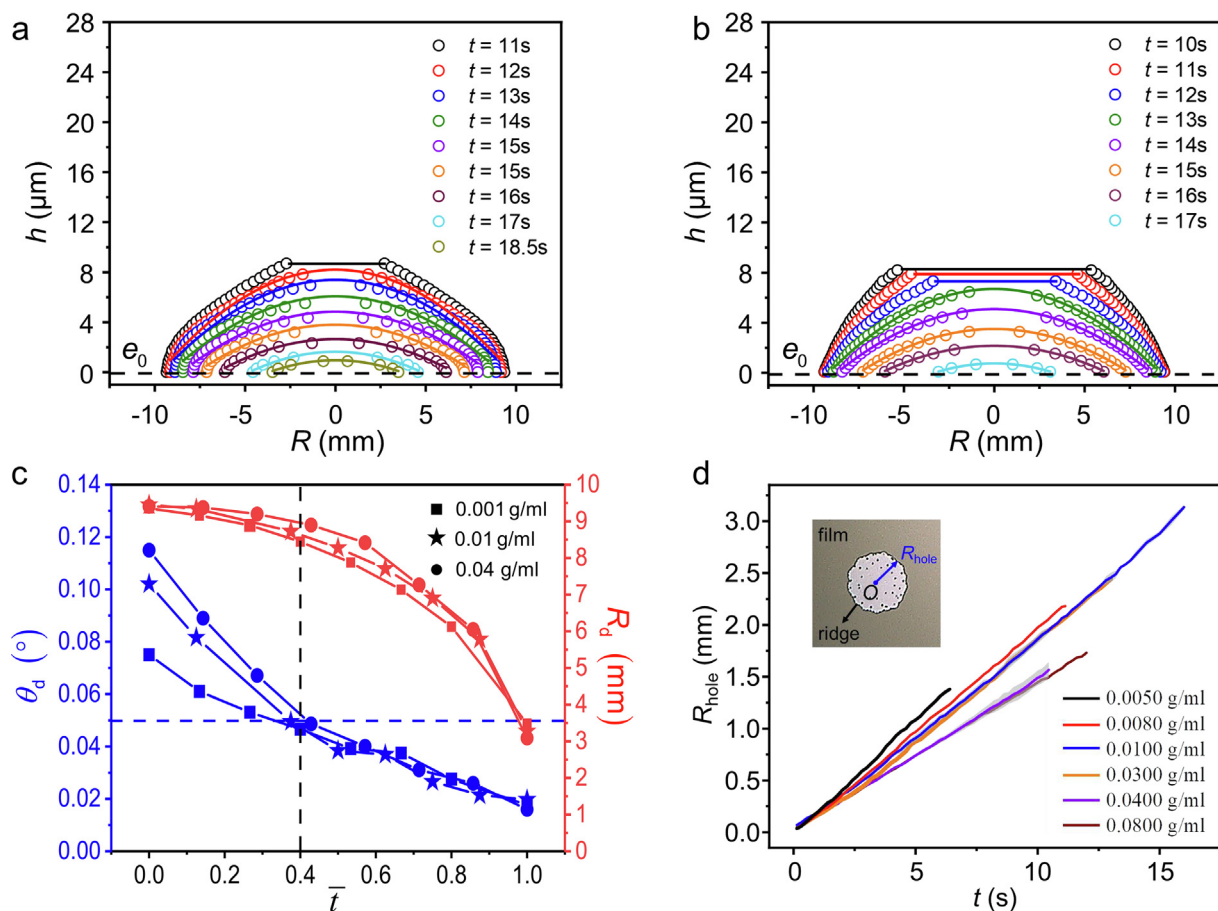


Fig. 4. Dewetting law of ethanol drops with different initial ibuprofen concentrations c_0 on the silicon wafer. Evolution of the profile $h(r,t)$ during drop dewetting at (a) $c_0 = 0.001$ and (b) 0.04 g mL^{-1} , where R and t denote position and time, respectively. (c) The contact angle θ_d and the contact radius R_d vary with dimensionless time \bar{t} , where \bar{t} represents the ratio of instantaneous time to total dewetting time. (d) During film dewetting, the hole expansion radius R_{hole} as a function of time t at different c_0 .

drop thins until it becomes a film. However, the film does not rupture, which is related to the thickness of the film (explained in detail later). During this period, ibuprofen particles deposit with the receding of the initial TPCL, as shown in the three typical ring patterns in Fig. 2d5 (red, green, and blue lines), finally forming the coffee ring (Fig. 2d6). It should be noted that the coffee ring mentioned in this work is composed of large-sized discrete ibuprofen particles (on the order of $10^2 \mu\text{m}$), so the spacing between particles is visible at the macroscopic scale. The ring pattern composed of dispersed particles (on the order of $10^{-1} \mu\text{m}$) reported in previous work appears to be continuous at the macroscopic scale [3,40,41], but when observed under the microscope, there is also spacing between the particles.

3.2. Fractal deposition patterns

The concentration dependency of the deposition patterns is probed in a series of experiments spanning four decades in the initial concentration of ibuprofen c_0 , which is a key parameter in this experiment (Fig. 5a). Consequently, several deposition patterns emerge under the same experimental model. According to the formation process (Fig. 2a–d) and the main features of patterns (Fig. 5b–e), we classify them into 3 types, i.e., uniform pattern, polygonal pattern, and coffee ring. At ultralow initial ibuprofen concentrations ($c_0 \leq 0.001 \text{ g mL}^{-1}$), ibuprofen is distributed on the entire initial solid–liquid contact area, forming a uniform pattern

(Fig. 5b). At high initial ibuprofen concentrations ($c_0 \geq 0.1 \text{ g mL}^{-1}$), ibuprofen precipitates and deposits around the receding TPCL, forming a ring-like pattern, as shown in the two typical ring patterns in Fig. 5e (orange and green lines). At intermediate initial ibuprofen concentrations ($0.001 < c_0 < 0.1 \text{ g mL}^{-1}$), the deposition patterns are presented in the form of polygons, where $c_0 = 0.01 \text{ g mL}^{-1}$ is a critical value distinguishing whether there are spiked depositions inside the polygons (Fig. 5c and d).

The uniform pattern is also composed of numerous small polygons at the microscale (the inset of Fig. 5b). In other words, as c_0 increases, the distance between polygons spans from the micrometer scale to the centimeter scale (Fig. 5a). In a later theoretical section, a model describing this distance is derived. The evolution in the geometry of the series of deposition patterns under different initial ibuprofen concentrations exhibits distinct multiscale properties, which is the most essential feature of the fractal phenomenon. The fractal dimension of the uniform pattern is 2, while that of the coffee ring is 1. The fractal dimensions of this series of deposition patterns, i.e., from uniform patterns to polygonal patterns, finally to coffee rings, transit from 2 to 1 through calculations (Fig. 5f). Under the same experimental model, the connection between the uniform pattern and coffee ring can be directly established by the fractal dimension, where polygonal patterns are the intermediate state. Hence, we name this series of deposition patterns “fractal deposition patterns”.

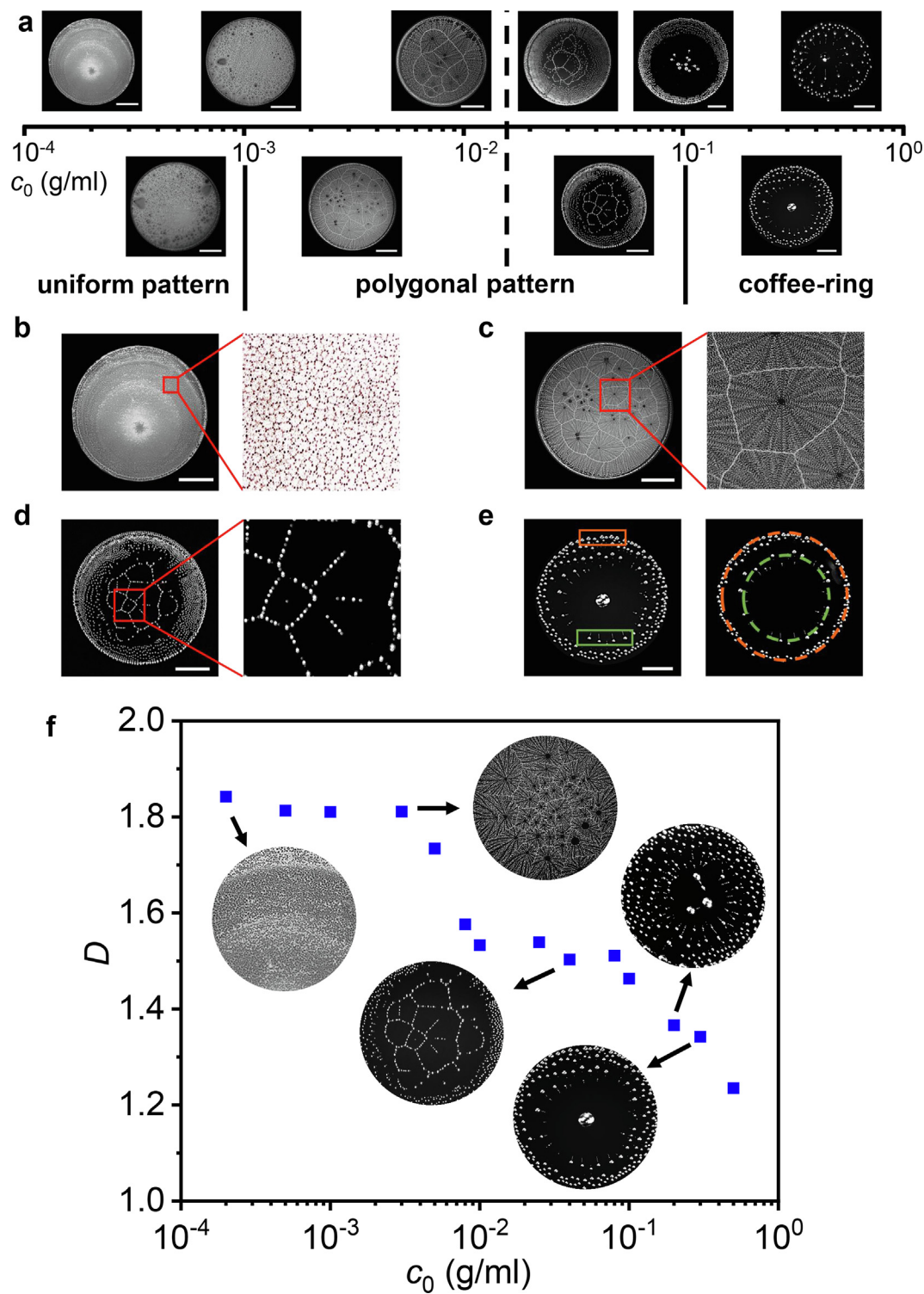


Fig. 5. Concentration dependence of the deposition patterns. (a) Evolution of deposition patterns as a function of initial ibuprofen concentration c_0 . (b), (c), (d), (e) Local details of the deposition patterns. The scale bars are all 5 mm. Deposition patterns are presented as a uniform distribution at ultralow concentrations, $c_0 \leq 0.001 \text{ g mL}^{-1}$ (b), and rings of discrete particles at high concentrations, $c_0 \geq 0.1 \text{ g mL}^{-1}$ (e). Between two extreme concentrations, $0.001 < c_0 < 0.1 \text{ g mL}^{-1}$, deposition patterns are presented as polygons, which are differentiated by spoked depositions inside the polygons (c, d). (f) Fractal dimensions D of deposition patterns at all initial ibuprofen concentrations c_0 in semilogarithmic coordinates. The fractal dimensions of the uniform pattern and coffee ring are considered to be 2 and 1, respectively. Through the calculations, the fractal dimensions of deposition patterns at different initial ibuprofen concentrations transition from 2 to 1, which creates a bridge between the uniform pattern and coffee ring. Hence, this series of deposition patterns is named “fractal deposition patterns”.

3.3. Theoretical model for the formation of fractal deposition patterns

Ethanol drops with different initial ibuprofen concentrations experience two main processes on the silicon wafer, i.e., spreading and dewetting, leaving films on the substrate.

Disturbance due to inertia exists on the film (Fig. S3), and the model of thickness fluctuations is simplified as a one-dimensional roughness profile, x (Fig. 6a) [42,43]. Hence, the expression of the free surface is written in the form

$$e(x, t) = e_0 + \delta e \exp(iqx) \exp(t/\tau), \quad (2)$$

where e_0 is the average thickness of the film, q is the wavenumber of the disturbance ($\lambda = 2\pi/q$ is its wavelength), and δe is its amplitude. τ is the relaxation time, characterizing the period from generation to instability or stability of the disturbance.

The curvature effect of the film surface creates a pressure modulation, which induces a flow J inside the film,

$$J = \frac{e_0^3}{3\eta} \left(-\frac{dp}{dx} \right), \quad (3)$$

where, η is the viscosity of the liquid, and $p = P''(e)e + (-\gamma_{LV}e'') + \rho g(e - z)$ (z represents any height position) is the sum of the long-range force, the Laplace pressure and gravity.

According to the conservation of volume,

$$\frac{\partial e}{\partial t} + \nabla J = 0. \quad (4)$$

Substituting Eqs. (2) and (3) into Eq. (4), the expression for the relaxation time τ is given, i.e., the governing equation

$$\frac{1}{\tau} = -\frac{e_0^3}{3\eta} [P''(e)q^2 + \gamma_{LV}q^4 + \rho gq^2]. \quad (5)$$

Measured by spectral ellipsometry, the average thickness of films e_0 spans from the order of 10^0 to 10^3 nm (details in the Experimental Section).

- i. For $e_0 > 10^3$ nm, the long-range force is negligible, and Eq. (5) becomes

$$\frac{1}{\tau} = -\frac{e_0^3}{3\eta} [\gamma_{LV}q^4 + \rho gq^2]. \quad (6)$$

Under the combined action of the surface tension and gravity, τ is always negative [6,44]. In other words, the surface tension and gravity eliminate the disturbance, making the film return to stability. The experimental results show that when $c_0 \geq 0.2$ g mL⁻¹, $e_0 > 10^3$ nm, and the film does not rupture, as shown in Fig. 7a.

- ii. For $10^2 < e_0 \ll 10^3$ nm, gravity can be ignored. Only the contribution of the surface tension needs to be considered. According to Eq. (6), τ is also negative, which implies that the film is stable. The experimental results show that when $c_0 = 0.1$ g mL⁻¹, $e_0 \approx 128$ nm, and the film does not rupture either, as shown in Fig. 7b.

- iii. For $e_0 < 10^2$ nm, the long-range force should be considered [26,44]. Here, we take into account the simple case of van der Waals force $P(e) = A/12\pi e^2$, where A is the Hamaker constant. Eq. (5) becomes

$$\frac{1}{\tau} = \frac{e_0^3 \gamma_{LV}}{3\eta} \left[-q^4 + \frac{q^2}{\xi_e^2} \right], \quad (7)$$

where, $\xi_e = (2\pi\gamma_{LV}/|A|)^{1/2} e_0^2$ is a characteristic length defined by the surface tension and the long-range force [42,45].

According to Eq. (7), the critical conditions for film instability are obtained. If $q\xi_e > 1$, τ is negative, and the fluctuation dies out. If $q\xi_e < 1$, τ is positive, and the fluctuation grows with time, causing spinodal decomposition. The film ruptures randomly, as shown in Fig. 7c.

The wavevector q_M of the fastest instability mode can be obtained by maximizing Eq. (7),

$$q_M = \frac{\sqrt{2}}{2\xi_e}. \quad (8)$$

Therefore, the corresponding wavelength is proportional to the square of the average thickness, $\lambda_M \propto e_0^2$. As shown in Fig. 7d, the experimental results are in good agreement with the theoretical prediction, where the experimental results are taken from the distance between the polygons.

During film dewetting, the average thickness is a key parameter that controls the film stability, which affects the final deposition patterns. This is also the first time that films with different thicknesses can be obtained easily in the same experimental model, allowing the verification of the theoretical model.

For polygonal patterns, the amplification of the disturbance leads to spinodal decomposition. Then, the thinnest regions of the film rupture, and a dry hole will appear, expanding on the substrate by forming a ridge (Fig. 2c5, 4d). Here, exploring the process of film dewetting requires explaining the motion of the ridge shown in Fig. 6b, and two hypotheses are proposed:

- (1) The cross section of the ridge is circular, and the dynamic contact angles θ at two contact lines (CL₁, CL₂) are the same.
- (2) The viscous dissipation is mainly dominated by the fluid flow within the ridge. The dynamics of thin films are generally dominated by viscous friction, so inertial effects can be ignored [44]. The van der Waals energy and the surface energy can be converted into viscous dissipation.

The motion of the ridge is controlled by an equilibrium between the driving force and the friction force. Considering the van der Waals force and the surface tension, the driving force F_d is written in the form

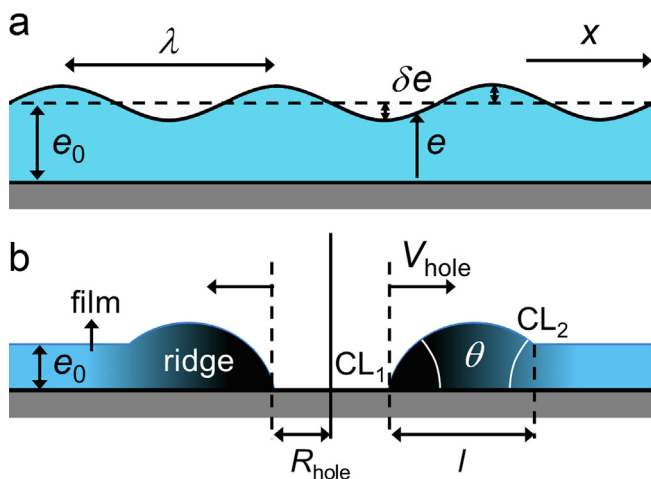


Fig. 6. Schematic illustration of the theoretical model. (a) Thickness fluctuation of the film considering evaporation. The film model is simplified as a one-dimensional roughness profile, x . (b) The hole expands on the substrate by forming a ridge, whose two contact lines (CL₁ and CL₂) are located on the dry silicon wafer and the wet film, respectively. Relevant parameters are the average thickness of the film e_0 , the thickness modulation of the film δe , the thickness of the film e , the wavelength of the disturbance λ , the expansion radius of the hole R_{hole} , the expansion velocity of the hole V_{hole} , the size of the ridge l , and the dynamical contact angle θ .

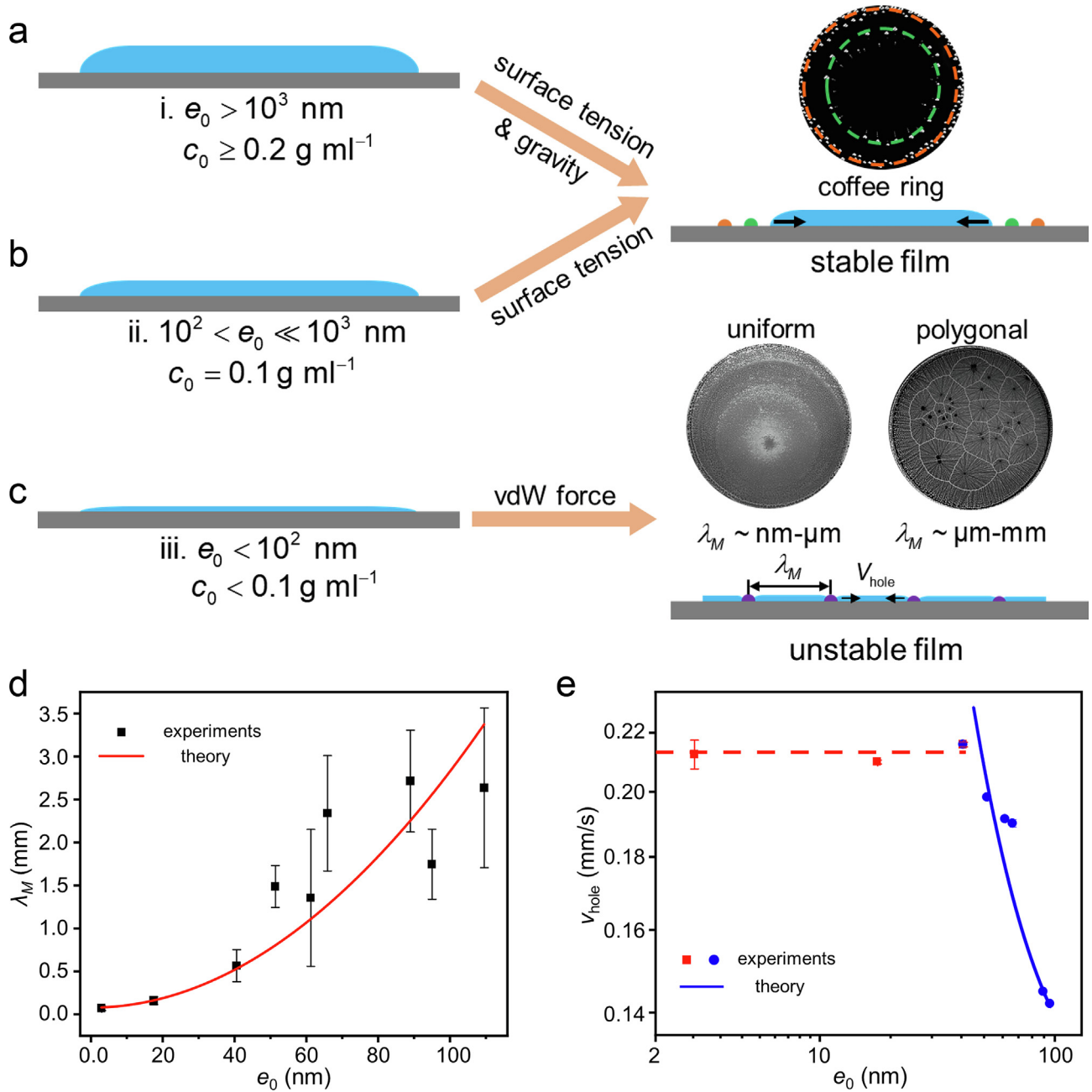


Fig. 7. Validation of the theoretical model. (a, b, and c) Schematic diagram for the stability analysis of films with different thicknesses. (d) Wavelength of the fast mode λ_M and (e) the expansion velocity of hole V_{hole} as a function of the average thickness of the film e_0 . The discrete dots and the solid lines represent the experimental results and the theoretical prediction, respectively, which shows that the experiments verify the theoretical model well.

$$F_d = \gamma_{SL} + \gamma_{LV} + P(e_0) + e_0\Pi(e_0), \quad (9)$$

where γ_{SL} and γ_{LV} are the surface tensions of the solid–liquid and the liquid–vapor interfaces, respectively. The term $P(e_0) + e_0\Pi(e_0)$ comes from the hydrostatic pressure generated by the van der Waals force, where $\Pi(e_0) = -dP/de_0$ is the disjoining pressure [42]. It follows that the ridge is pulled by a force related to the average film thickness.

The friction force F_v is exerted by the movement of the ridge on the substrate. The friction force on CL₁ is $F_{v1} = (3\eta V_{CL1} \ln_{CL1})/\theta$ and on CL₂ is $F_{v2} = (3\eta V_{CL2} \ln_{CL2})/\theta$, where η is the viscosity and V_{CL1} and V_{CL2} are the velocities of CL₁ and CL₂, respectively. \ln_{CL1} and \ln_{CL2} denote the divergence of the viscous dissipation. Since dl/dt

is much smaller than the hole expansion velocity V_{hole} , $V_{CL1} = V_{CL2}$ is assumed.

Hence, the friction force F_v has the form of

$$F_v = \frac{6\eta V \ln T}{\theta}, \quad (10)$$

where $\ln T$ denotes the divergence of the viscous dissipation at the ridge.

Combining Eqs. (9) and (10), we can obtain

$$V_{hole} = \frac{\gamma\theta}{6\eta \ln T} + \frac{A\theta}{24\pi\eta \ln T} e_0^{-2}, \quad (11)$$

where γ is the contribution of surface tension of solid–liquid and liquid–vapor interfaces.

This indicates that the hole expansion velocity is related to the average film thickness of the same liquid. For a constant thickness film, the expansion velocity is a constant, which agrees with the experimental results (Fig. 4d). For films with variable thickness, the expansion velocity is proportional to the negative square of the average thickness, $V_{\text{hole}} \propto e_0^{-2}$. As shown in Fig. 7e, the experimental results (blue dots) are consistent with the theoretical prediction (blue solid line). Notably, for thin films ($< 40\text{nm}$), the expansion velocity is a constant remaining at approximately 0.215 mm s^{-1} (red square and red dotted line). This is because when the film becomes very thin ($e_0 \rightarrow 0$), the energy of the bare substrate (solid–vapor surface energy) must be recovered, which is necessary to consider the contribution of the long-range force.

4. Conclusion

We adopt a simple but ingenious strategy to construct self-assembled patterns, which for the first time directly establishes the connection between the uniform pattern and the coffee ring under the same physics. An ethanol drop with dissolved ibuprofen was deposited on a smooth silicon wafer. Unlike aqueous solutions of dispersed particles chosen in most studies, such as polystyrene (PS) particles [19,46–48], ibuprofen can be readily dissolved in rapidly volatile ethanol, where the ibuprofen–ibuprofen, ethanol–ethanol, and ibuprofen–ethanol interactions can be adapted automatically with the rapid evaporation of ethanol. As a result, the size and deposition process of ibuprofen particles can be controlled more intelligently. The uncertainty caused by the artificial modification of particles in experiments is avoided, greatly improving the accuracy and repeatability. Just changing one key parameter, i.e., the initial ibuprofen concentration c_0 , uniform pattern, polygonal pattern, and coffee ring can be achieved under the same experimental model. We carefully analyze the rich behaviors of the drops on the silicon wafer, i.e., spreading, evaporative instability, dewetting, film formation, and particle deposition. From a macroscopic perspective, this series of deposition patterns is essentially composed of several polygons with different characteristic sizes (nm–cm), where the multiscale property clearly exhibited in the geometry prompts us to successfully establish the bridge connecting a uniform pattern and coffee ring through the fractal dimension. Therefore, this series of patterns under the same experimental model is named “fractal deposition patterns”. A theoretical model considering film stability is established to explain the mechanism behind pattern formation, which is well verified by experiments.

Our study provides new insight into the field of interface science, completely different from the previous routes of evaporation-induced self-assembly [3,12,13]. Although the solute–solvent combination is specific, this series of self-assembled patterns is quite general and has been demonstrated to have broad application prospects [7–9]. Therefore, we expect that these results may provide a low-cost method for making specific patterns for other particles or macromolecule deposition on specific surfaces. In addition, the nonlinear relationship between the scaling exponent and the solute concentration in drop spreading lacks quantitative study, although the Marangoni effect is believed to be the cause of rapid spreading. However, these investigations are left for further studies.

CRediT authorship contribution statement

Fushuai Wang: Conceptualization, Methodology, Investigation, Writing – original draft. **Quanzi Yuan:** Conceptualization, Methodology, Writing – review & editing, Supervision, Project administration, Funding acquisition.

Data availability

Data will be made available on request.

Declaration of Competing Interest

The authors declare that they have no known competing financial interests or personal relationships that could have appeared to influence the work reported in this paper.

Acknowledgment

This work was jointly supported by the National Natural Science Foundation of China (NSFC, Grant Nos. 12072346, 12032019).

Appendix A. Supplementary data

Supplementary data to this article can be found online at <https://doi.org/10.1016/j.jcis.2023.01.102>.

References

- [1] R.G. Picknett, R. Bexon, The evaporation of sessile or pendant drops in still air, *J. Colloid Interface Sci.* 61 (1977) 336–350.
- [2] A.G. Marín, H. Gelderblom, D. Lohse, J.H. Snoeijer, Order-to-disorder transition in ring-shaped colloidal stains, *Phys. Rev. Lett.* 107 (2011) 085502.
- [3] R.D. Deegan, O. Bakajin, T.F. Dupont, G. Huber, S.R. Nagel, T.A. Witten, Capillary flow as the cause of ring stains from dried liquid drops, *Nature* 389 (1997) 827–829.
- [4] R.D. Deegan, O. Bakajin, T.F. Dupont, G. Huber, S.R. Nagel, T.A. Witten, Contact line deposits in an evaporating drop, *Phys. Rev. E* 62 (2000) 756–765.
- [5] G. Reiter, Dewetting of thin polymer films, *Phys. Rev. Lett.* 68 (1992) 75.
- [6] G. Reiter, Unstable thin polymer films: Rupture and dewetting processes, *Langmuir* 9 (1993) 1344–1351.
- [7] J. Pyeon, K.M. Song, Y.S. Jung, H. Kim, Self-induced solutal marangoni flows realize coffee-ring-less quantum dot microarrays with extensive geometric tunability and scalability, *Adv. Sci.* 9 (2022) 2104519.
- [8] M. Singh, H.M. Haverinen, P. Dhagat, G.E. Jabbour, Inkjet printing process and its applications, *Adv. Mater.* 22 (2010) 673–685.
- [9] H. Kim, F. Boulogne, E. Um, I. Jacobi, E. Button, H.A. Stone, Controlled uniform coating from the interplay of marangoni flows and surface-adsorbed macromolecules, *Phys. Rev. Lett.* 116 (2016) 124501.
- [10] P.J. Yunker, T. Still, M.A. Lohr, A. Yodh, Suppression of the coffee-ring effect by shape-dependent capillary interactions, *Nature* 476 (2011) 308–311.
- [11] P. Galliker, J. Schneider, H. Eghlidi, S. Kress, V. Sandoghdar, D. Poulikakos, Direct printing of nanostructures by electrostatic autofocussing of ink nanodroplets, *Nat. Commun.* 3 (2012) 890.
- [12] H. Hu, R.G. Larson, Marangoni effect reverses coffee-ring depositions, *J. Phys. Chem. B* 110 (2006) 7090–7094.
- [13] Y.P. Zhao, *Physical mechanics of surfaces and interfaces*, Science Press, Beijing, 2012.
- [14] A. Matavž, U. Uršič, J. Močivnik, D. Richter, M. Humar, S. Čopar, B. Malič, V. Bobnar, From coffee stains to uniform deposits: Significance of the contact-line mobility, *J. Colloid Interface Sci.* 608 (2022) 1718–1727.
- [15] H.J. Butt, R. Berger, W. Steffen, D. Vollmer, S.A.L. Weber, Adaptive wetting adaptation in wetting, *Langmuir* 34 (2018) 11292–11304.
- [16] S.J. Kim, K.H. Kang, J.G. Lee, I.S. Kang, B.J. Yoon, Control of particle deposition pattern in a sessile droplet by using radial electroosmotic flow, *Anal. Chem.* 78 (2006) 5192–5197.
- [17] K.N. Al-Milaji, V. Radhakrishnan, P. Kamerkar, H. Zhao, pH-modulated self-assembly of colloidal nanoparticles in a dual-droplet inkjet printing process, *J. Colloid Interface Sci.* 529 (2018) 234–242.
- [18] K.N. Al-Milaji, R.R. Secondo, T.N. Ng, N. Kinsey, H. Zhao, Interfacial self-assembly of colloidal nanoparticles in dual-droplet inkjet printing, *Adv. Mater. Interfaces* 5 (2018) 1701561.
- [19] F.S. Wang, S.H. Tian, Q.Z. Yuan, Evaporation-induced crystal self-assembly (EICSA) of salt drops regulated by trace of polyacrylamide, *Colloids Surf. A Physicochem. Eng. Asp.* 644 (2022) 128856.
- [20] R. Iqbal, A. Matsumoto, D. Carlson, K.T. Peters, R. Funari, A.K. Sen, A.Q. Shen, Evaporation driven smart patterning of microparticles on a rigid-soft composite substrate, *J. Colloid Interface Sci.* 623 (2022) 927–937.
- [21] R. Iqbal, A. Atsushi Matsumoto, A.Q. Sudeepthi, A.K.S. Shen, Substrate stiffness affects particle distribution pattern in a drying suspension droplet, *Appl. Phys. Lett.* 114 (25) (2019) 253701.
- [22] J. Gerber, T.M. Schutzius, D. Poulikakos, Patterning of colloidal droplet deposits on soft materials, *J. Fluid Mech.* 907 (2021) A39.

- [23] D.Y. Zang, S. Tarafdar, Y.Y. Tarasevich, M. Dutta Choudhury, T. Dutta, Evaporation of a droplet: From physics to applications, *Phys. Rep.* 804 (2019) 1–56.
- [24] M. Majumder, C.S. Rendall, J.A. Eukel, J.Y.L. Wang, N. Behabtu, C.L. Pint, T.Y. Liu, A.W. Orbaek, F. Mirri, J. Nam, et al., Overcoming the “coffee-stain” effect by compositional marangoni-flow-assisted drop-drying, *J. Phys. Chem. B* 116 (2012) 6536–6542.
- [25] A.D. Carrithers, M.J. Brown VI, M.Z. Rashed, S. Islam, O.D. Velev, S.J. Williams., Multiscale self-assembly of distinctive weblike structures from evaporated drops of dilute american whiskeys, *ACS Nano* 14 (2020) 5417–5425.
- [26] A.P. Mouat, C.E. Wood, J.E. Pye, J.C. Burton, Tuning contact line dynamics and deposition patterns in volatile liquid mixtures, *Phys. Rev. Lett.* 124 (2020) 064502.
- [27] L. Keiser, H. Bense, P. Colinet, J. Bico, E. Reyssat, Marangoni bursting: Evaporation-induced emulsification of binary mixtures on a liquid layer, *Phys. Rev. Lett.* 118 (2017) 074504.
- [28] T. Still, P.J. Yunker, A.G. Yodh, Surfactant-induced marangoni eddies alter the coffee-rings of evaporating colloidal drops, *Langmuir* 28 (2012) 4984–4988.
- [29] C.D. Bain, G.D. Burnett-Hall, R.R. Montgomerie, Rapid motion of liquid drops, *Nature* 372 (1994) 414–415.
- [30] Q.Z. Yuan, X.F. Huang, Y.P. Zhao, Dynamic spreading on pillar-arrayed surfaces: Viscous resistance versus molecular friction, *Phys. Fluids* 26 (2014) 092104.
- [31] P. Kavehpour, B. Ovryn, G.H. McKinley, Evaporatively-driven Marangoni instabilities of volatile liquid films spreading on thermally conductive substrates, *Colloids Surf. A* 206 (2002) 409–423.
- [32] D. Bonn, J. Eggers, J. Indekeu, J. Meunier, E. Rolley, Wetting and spreading, *Rev. Mod. Phys.* 81 (2009) 739–805.
- [33] A.E. Hosoi, J.W.B. Bush, Evaporative instability in climbing films, *J. Fluid. Mech.* 442 (2001) 217–239.
- [34] S. Rafai, D. Sarker, V. Bergeron, J. Meunier, D. Bonn, Superspreading: Aqueous surfactant drops spreading on hydrophobic surfaces, *Langmuir* 18 (2002) 10486–10488.
- [35] B. David, *Droplet wetting and evaporation*, Academic Press, 2015.
- [36] S.F. Zhang, W.L. Luan, Q.X. Zhong, S.F. Yin, F.Q. Yang, Evaporation-induced self-assembly of quantum dots-based concentric rings on polymer-based nanocomposite films, *Soft Matt.* 12 (2016) 8285–8296.
- [37] F. Wodlei, J. Sebilliau, J. Magnaudet, V. Pimienta, Marangoni-driven flower-like patterning of an evaporating drop spreading on a liquid substrate, *Nat. Commun.* 9 (2018) 820.
- [38] J. Eggers, Nonlinear dynamics and breakup of free-surface flows, *Rev. Mod. Phys.* 69 (1997) 865.
- [39] Y. Gotkis, I. Ivanov, N. Murisic, L. Kondic, Dynamic structure formation at the fronts of volatile liquid drops, *Phys. Rev. Lett.* 97 (2006) 186101.
- [40] F.S. Wang, M.M. Wu, X.K. Man, Q.Z. Yuan, Formation of deposition patterns induced by the evaporation of the restricted liquid, *Langmuir* 36 (2020) 8520–8526.
- [41] M. Rey, J. Walter, J. Harrer, C.M. Perez, S. Chiera, S. Nair, M. Ickler, A. Fuchs, M. Michaud, M.J. Uttinger, A.B. Schofield, J.H.J. Thijssen, M. Distaso, W. Peukert, N. Vogel, Versatile strategy for homogeneous drying patterns of dispersed particles, *Nat. Commun.* 13 (2022) 2840.
- [42] F.B. Wyart, J. Daillant, Drying of solids wetted by thin liquid films, *Can. J. Phys.* 68 (1990) 1084–1088.
- [43] M.B. Williams, S.H. Davis, Nonlinear theory of film rupture, *J. Colloid Interface Sci.* 90 (1982) 220.
- [44] P.G. de Gennes, F. Brochard-Wyart, D. Quere, *Capillarity and wetting phenomena, drops, bubbles, pearls, waves*, Springer-verlag, 2004.
- [45] D. Andelman, J.F. Joanny, M.O. Robbins, Complete wetting on rough surfaces: Static, *Europhys. Lett.* 7 (1988) 731.
- [46] L. Cui, Y. Han, Honeycomb pattern formation via polystyrene/poly (2-vinylpyridine) phase separation, *Langmuir* 21 (2005) 11085–11091.
- [47] Z.S. Davidson, Y.Y. Huang, A. Gross, A. Martinez, T. Still, C. Zhou, P.J. Collings, R. D. Kamien, A.G. Yodh, Deposition and drying dynamics of liquid crystal droplets, *Nat. Commun.* 8 (2017) 15642.
- [48] H. Zargartalebi, S.H. Hejazi, A. Sanati-Nezhad, Self-assembly of highly ordered micro- and nanoparticle deposits, *Nat. Commun.* 13 (2022) 3085.